Chemistry–A European Journal
Research Article
doi.org/10.1002/chem.202403574
Chemistry Europe
European Chemical Societies Publishing
www.chemeurj.org

Hot Paper

Experimental and Theoretical Insights on Gas Trapping of Noble Gases in MFU-4-Type Metal–Organic Frameworks

Hana Bunzen,*[a] Beliz Sertcan Gökmen,[b] Andreas Kalytta-Mewes,[a] Maciej Grzywa,[c] Jakub Wojciechowski,[c] Jürg Hutter,[b] Anna-Sophia Hehn,[b, d] and Dirk Volkmer*[a]

Isostructural metal–organic frameworks (MOFs), namely MFU-4 and MFU-4-Br, in which the pore apertures are defined by anionic side ligands (Cl^- and Br^-, respectively), were synthesized and loaded with noble gases. By selecting the type of side ligand, one can fine-tune the pore aperture size, allowing for precise regulation of the entry and release of gas guests. In this study, we conducted experiments to examine gas loading and release using krypton and xenon as model gases, and we complemented our findings with computational modeling. Remarkably, the loaded gas guests remained trapped inside the pores even after being exposed to air under ambient conditions for extended periods, in some cases for up to several weeks. Therefore, we focused on determining the energy barrier preventing gas release using both theoretical and experimental methods. The results were compared in relation to the types of hosts and guests, providing valuable insights into the gas trapping process in MOFs, as well as programmed gas release in air under ambient conditions. Furthermore, the crystal structure of MFU-4-Br was elucidated using the three-dimensional electron diffraction (3DED) technique, and the bulk purity of the sample was subsequently verified through Rietveld refinement.

Introduction

Metal–organic frameworks (MOFs)[1] are crystalline porous coordination polymers with attractive properties, with porosity being a key feature,[2] reaching up to around 7800 $m^2 g^{-1}$.[3] This intrinsic characteristic makes MOFs highly suitable for gas storage and separation applications.[4] The effectiveness of MOFs in these processes significantly depends on their structural properties. Various strategies have been devised to enhance the sorption properties for specific gases.[5] For instance, Guo *et al.* demonstrated the use of MOFs with pores featuring exposed metal ions capable of distorting the electron cloud of methane, leading to polarization and enhanced gas adsorption.[6] McDonald *et al.* explored the use of diamine-appended metal–organic frameworks as CO_2 adsorbents in gas separation, showcasing the insertion of CO_2 molecules into metal-amine bonds, thereby enhancing the material's adsorption capabilities.[7]

Another intriguing approach to gas storage in MOFs is the strategy presented in this study, focusing on MOFs with narrow pore apertures smaller than the size of the gas guest. In this process, the gas guest is introduced into the pores under specific loading conditions and is not released immediately under ambient conditions. As a proof-of-concept investigation, we recently reported on xenon storage in a MOF known as MFU-4,[8] demonstrating the feasibility of storing significant quantities of gas (larger than 40 wt%) within the voids, even when the material was exposed to air under ambient conditions.[9] In follow-up studies we investigated the approach on an example of sulfur hexafluoride as a guest trapped in the pores of MOFs MFU-4[10] and ZIF-8.[11] Herein, considering the practically boundless MOF design possibilities,[12] we delve into an exploration of the gas storage properties of the MOF MFU-4 by tailoring its structural characteristics and incorporating diverse gas guests, namely krypton and xenon, and examine such systems comprehensively through a combination of experimental and theoretical methods. Our aim is to formulate the system properties required to achieve effective gas trapping.

MFU-4 is an example of a benzobistriazolate-based MOF and belongs to the 'MFU-4-type' frameworks previously reported by us.[8,13] MOFs of this family have been investigated for various applications, including H_2/D_2 separation,[14] binding and activation of small molecules,[15] catalysis,[16] enzyme mimetics,[17] or drug delivery.[18] The 'MFU-4-type' frameworks comprise pentanuclear secondary building units with a general formula $[M^{II}{}_5X_4(L^{-2})_3]$. Within the pentanuclear coordination unit (Figure 1b), the central $metal^{II}$ ion adopts an octahedral geometry (M^{oct}), coordinated to six bis(triazolate) ligands (L^{-2}).

[a] H. Bunzen, A. Kalytta-Mewes, D. Volkmer
Chair of Solid State and Materials Chemistry, Institute of Physics, University of Augsburg, Universitätsstraße 1, 86159 Augsburg, Germany
E-mail: hana.bunzen@physik.uni-augsburg.de
dirk.volkmer@physik.uni-augsburg.de

[b] B. Sertcan Gökmen, J. Hutter, A.-S. Hehn
Department of Chemistry, University of Zurich, Winterthurerstrasse 190, 8057 Zurich, Switzerland

[c] M. Grzywa, J. Wojciechowski
Rigaku Europe SE, Hugenottenallee 167, 63263 Neu-Isenburg, Germany

[d] A.-S. Hehn
Institute of Physical Chemistry, Christian-Albrechts-University Kiel, Max-Eyth-Strasse 1, 24118 Kiel, Germany

Supporting information for this article is available on the WWW under https://doi.org/10.1002/chem.202403574

Table 1. Selected structural parameters of MFU-4 and MFU-4-Br obtained from experimental data.

MOF	a, b and c (Å)	Unit cell volume (Å^3)	Pore aperture (Å)	Kinetic diameter (Xe)/ Pore aperture	Kinetic diameter (Kr)/ Pore aperture
MFU-4	21.697(3)[a]	10214(2)[a]	2.53[b]	3.96/2.53 = 1.57	3.60/2.53 = 1.42
MFU-4-Br	21.71314(11)[c] 21.7110(10)[d]	10236.9[c] 10233.9[d]	2.15[b]	3.96/2.15 = 1.84	3.60/2.15 = 1.67

[a] Data from ref. [8] [b] Determined by the Pore Analyser function in the software Mercury by the Cambridge Crystallographic Data Centre (Figure S6). [c] From Rietveld refinement;[21] for details see Supporting Information. [d] From an electron diffraction measurement;[21] for details see Supporting Information.

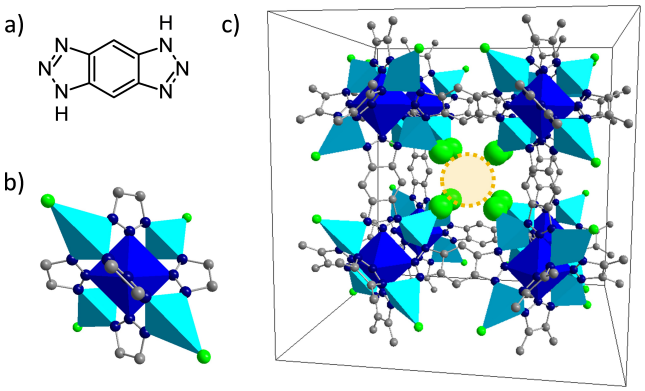

Figure 1. A structure of the (a) benzobistriazole ligand [1H,5H-benzo(1,2-d:4,5-d′)bistriazole], (b) pentanuclear coordination unit featuring the central Zn^{II} ion in an octahedral geometry (dark blue) and four Zn^{II} ions in a tetrahedral coordination environment (turquoise), and (c) unit cell of MFU-4 (CCDC: 723714) with a pore aperture visualized as a yellow circle. Elements: C (grey), H (white), N (blue), Cl (green), Zn^{oct} (dark blue), Zn^{tetr} (turquoise).

The remaining four peripheral $metal^{II}$ ions feature a tetrahedral coordination environment (M^{tetr}), and each of them is bound to three *N*-donor atoms from three different bis(triazolate) ligands and to one additional monodentate (anionic) ligand (X^-). MFU-4 is constructed with benzobistriazole ligands [specifically 1H,5H-benzo(1,2-d:4,5-d′)bistriazole] and Zn^{II} cations (Figure 1), featuring two types of voids of 3.9 and 11.94 Å.[8] These small and large pores are connected by 2.53 Å narrow pore apertures (Table 1). The MOF possesses a highly adaptable structure for customizing the size of its aperture. This versatility arises from the fact that the pore aperture is defined by four chlorido ligands (Figure 1c). Consequently, it can be modified by introducing other anionic ligands of varying sizes, such as different halides, as demonstrated in this work through the synthesis of a new MOF MFU-4-Br. Besides this new MOF, variants with hydroxide and fluorido side ligands (i.e., MFU-4-OH and MFU-4-F) are also known.[19] However, unlike these two MOFs, which were prepared via postsynthetic ligand exchange, MFU-4-Br reported here is prepared via direct synthesis.

Results and Discussion

Material Synthesis

MFU-4 is prepared by mixing 1H,5H-benzo(1,2-d:4,5-d′)bistriazole and anhydrous zinc chloride in DMF. The sample can be heated either conventionally at 145 °C for 3 days, or by microwave irradiation at 155 °C for 10 min at 300 W.[8] By tuning the reaction conditions, the crystal size and morphology can be addressed.[20] By applying the reported procedure for the synthesis of MFU-4 and using $ZnBr_2$ instead of $ZnCl_2$ as a metal salt, an isostructural analogue was prepared, here called MFU-4-Br, comprising bromido side ligands (instead of the chlorido ligands). The newly synthetized MFU-4-Br was characterized by scanning electron microscopy (SEM), thermogravimetric analysis (TGA), (variable temperature) X-ray powder diffraction (XRPD) measurements and Fourier-transform infrared spectroscopy (FTIR), and the data were compared to the analyses of MFU-4 (Figures S1–S4).

As revealed by scanning electron microscopy, both materials were prepared as 1–10 μm large cubic crystals (Figures 2a and S1). The structure of MFU-4 was elucidated in prior studies utilizing X-ray powder diffraction data and *ab-initio* structure determination methods (CCDC: 723714).[8] Despite extensive efforts and modifications to the synthesis parameters (refer to Experimental section for details), we were unable to obtain single crystals exceeding 10 μm in size. Therefore, the structure of MFU-4-Br was elucidated by electron diffraction (Tables S1–S7) and the phase purity of the bulk sample was confirmed by the Rietveld refinement (Figure S5).[21] MFU-4-Br is isostructural to MFU-4. Selected structural parameters of both MOFs can be found in Table 1 and Figure S6.

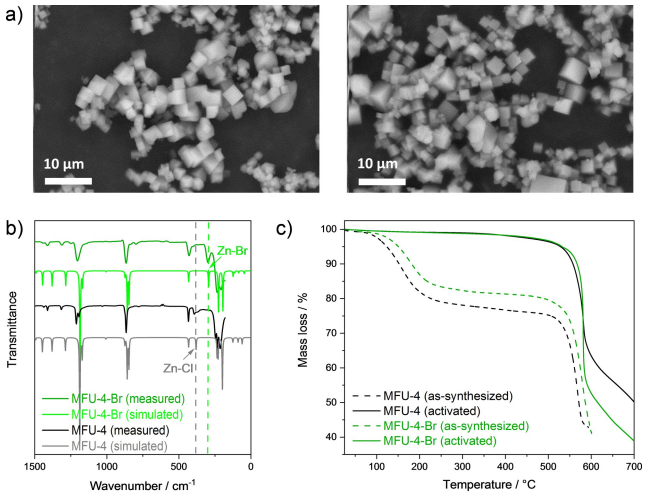

Figure 2. (a) SEM micrographs of MFU-4 (right) and MFU-4-Br (left), (b) experimental FTIR data and simulated[a] IR spectra, and (c) TGA curves of as-synthetized and activated samples.

Table 2. Overview of gas loading under various conditions determined by thermogravimetric analysis. For complete data, see Figures S7–S10 and Tables S8–S11.

Guest	MOF	Sample no.	Gas pressure (bar)	Temp. (°C)	Time (h)	Gas loaded (wt%)	No. of gas atoms per unit cell	No. of gas atoms per pore
Xe	MFU-4	1	30	100	18	42.8	42.9	10.7
		2	30	100	48	44.5	46.1	11.5
Kr	MFU-4	4	50	RT	18	20.9	23.7	5.9
Xe	MFU-4-Br	8	30	200	18	25.4	23.3	5.9
		9	30	200	48	29.4	28.5	7.1
Kr	MFU-4-Br	12	50	50	18	23.8	33.4	8.3

When comparing the FTIR spectra of both MOFs, the characteristic Zn–X bands (X stands either for Cl or Br) were detected and the position of these bands agreed with their corresponding simulated IR spectra (Figures 2b and S4). The material thermal stability was studied by TGA and variable temperature XRPD (Figures 2c and S3). The analyses revealed that both MOFs were stable up to more than 500 °C (under nitrogen atmosphere), and that the removal of the solvent from the pores did not affect the structure as confirmed by the variable temperature XRPD measurements (Figure S3). This means that the MOF voids could be emptied and made accessible for potential guest molecules.

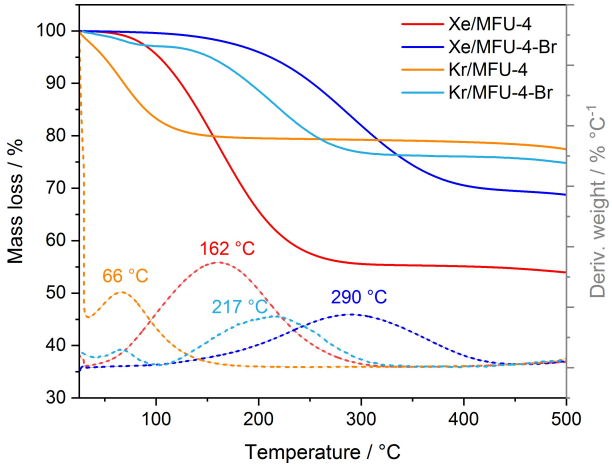

Figure 3. Thermogravimetric analysis of selected samples (Sample 2, 4, 9 and 12, Table 2); the measurement was carried out under a nitrogen atmosphere with a heating rate of 10 K min^{-1}; the weight derivation as a function of temperature is depicted as dotted lines with temperature of maximum gas release indicated. [a] Data simulated with the CASTEP code as part of BIOVIA Materials Studio, rel. 2018.[22]

Gas Loading Studies

Gas loading and release from MFU-4 and MFU-4-Br were investigated using xenon and krypton as model gas guests, with kinetic diameters of 3.96 and 3.60 Å, respectively.[23] Our aim was to correlate the influence of the ratio between the guest kinetic diameter and the pore aperture size on the gas loading. Depending on the guest-material pair, the guest was between 1.42 to 1.84 times larger than the MOF pore aperture and for the ratio, the following trend could be concluded: Kr/MFU-4 < Xe/MFU-4 < Kr/MFU-4-Br < Xe/MFU-4-Br (Table 1).

The influence of various loading conditions, such as pressure, temperature and time, on the xenon loading into MFU-4 was studied previously in detail.[9] Herein we compared the optimized loading conditions to the conditions needed to load krypton into MFU-4, and krypton and xenon into MFU-4-Br. The amount of the loaded gas was quantified by TGA (Figures S7–S10 and Tables S8–S11). The loading results clearly indicate that the size of the guest and the pore aperture has an impact on the optimal loading conditions (Table 2). Generally, it can be concluded that the higher the ratio of guest size to pore aperture size, the higher loading temperature is needed to load comparably high amounts of the gas guest. For instance, the highest amount of xenon loaded into MFU-4 was achieved at 30 bar at 100 °C, while for the loading of xenon into MFU-4-Br, a loading temperature of 200 °C was needed. Moreover, thermogravimetric analysis also revealed that the larger the guest in comparison to the pore aperture size, the higher temperature of the maximal gas release was (Figure 3).

These findings indicate that the activation energy barrier of the guest release from the pores depends on the guest-pore aperture size ratio. For instance, it can be expected that the activation energy barrier of gas release from MFU-4 is lower in comparison to the activation energy of the same gas guest loaded into the pores of MFU-4-Br. This has been further confirmed by experimental and computational studies and is discussed in detail later in this article.

Furthermore, successful loading was also confirmed by recording XRPD patterns. The intensities of the diffraction peaks changed in both samples when loaded with either krypton or xenon (Figures S12, S14, S16 and S18). This change in intensity is primarily attributed to the alteration of the electronic environment within the pores caused by the presence of these electron-rich gases. Over time, as the gas guests are released, the intensity of the diffraction peaks gradually returns to its original state, indicating a recovery of the structural integrity of the MOFs.

Gas Release and Experimental Determination of the Activation Energy

Considering the different guest sizes (kinetic diameter of Xe: 3.96 Å, kinetic diameter of Kr: 3.60 Å),[23] one could expect the impact of this parameter on the gas release kinetics to be significant. And indeed, the smaller the guest, the faster the guest release was observed (Figure 4). For the systems with krypton as a guest, i.e. Kr/MFU-4 and Kr/MFU-4-Br, the gas was released within few hours and few days, respectively, if the samples were exposed to air under ambient conditions (Figures S13 and S17, and Tables S13 and S15). However, in the case of the other two samples, i.e. Xe/MFU-4 and Xe/MFU-4-Br, the release was much more gradual and even after several weeks, a significant amount of the gas remained in the pores (Figures S11 and S15, and Tables S12 and S14). For instance, after 42 days approximately 27% of the originally loaded xenon remained in the pores of MFU-4, and 68% in the case of MFU-4-Br.

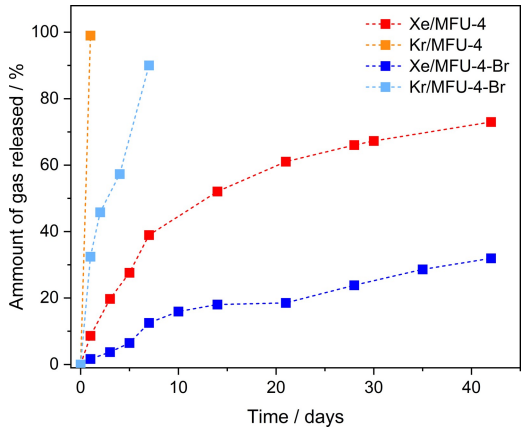

Figure 4. Gas release from samples exposed to air under ambient conditions determined by thermogravimetric analysis (Figures S11, S13, S15 and S17, and Tables S12–S15).

Although it is possible to compare the gas release curves of krypton in MFU-4 with the release curves of xenon in MFU-4, and the gas release curves of krypton in MFU-4-Br with the release curves of xenon in MFU-4-Br, it is not straightforward to compare the results of MFU-4 with MFU-4-Br. Since the gas release is a diffusion process, the size of the MOF crystals matters (as we reported recently on an example of ZIF-8 of various sizes loaded with SF_6[11]) and thus, since both samples are not identical in their particle size, their gas release curves should not be directly compared. Therefore, in order to compare both MOF systems with each other, the activation energy barrier of the guest release was determined both experimentally and computationally.

The activation energy barrier of the guest release was determined experimentally by carrying out modulated thermogravimetric analysis (MTGA™ by TA instruments). Modulated TGA uses an oscillation temperature program to obtain kinetic parameters during mass loss.[24] Herein the studies revealed that activation of xenon release from MFU-4 and MFU-4-Br was ca. 67 ± 1 and 92 ± 2 kJ mol^{-1}, respectively, while the activation energy of krypton release from MFU-4-Br was ca. 75 ± 4 kJ mol^{-1} (Table 3, Figure S19). Since the release of krypton from MFU-4 occurs relatively rapidly already at ambient temperature, an alternative approach for determining the activation energy had to be utilized. We measured gas release curves from −100 to 300 °C at different heating rates (1, 3, 5, and 7 K min^{-1}) (Figure S20) and used these data to determine the activation energy (Figure S21), which was approximately 53 ± 9 kJ mol^{-1}. The determined values of activation energy are in good agreement with the guest-pore aperture size ratio (Table 1)

Table 3. Overview of activation energies (in kJ mol^{-1}) for the different guest-MOF pairs determined by computational and experimental methods. In computational studies, the guest atom crosses the small to large pore barrier (sp- > lp) and large to small pore barrier (lp- > sp).

	Methods	Pore barrier	Kr/Cl Activ. energy	Xe/Cl Activ. energy	Kr/Br Activ. energy	Xe/Br Activ. energy
Exp.	MTGA	–	–	67.48 ± 0.51	74.92 ± 3.87	92.03 ± 1.74
	Variable heat. rates	–	53.03 ± 9.39	–	–	–
Calc.	PBEsol	sp- > lp	–	51	–	–
	Ref. [9]	lp- > sp	46	66	–	–
	ωB97X-2	sp- > lp	–	52	–	–
	Ref. [9]	lp- > sp	–	79	–	–
	NEB	sp- > lp	40.2	55.8	74.2	58.6
	(PBEsol)	lp- > sp	42.9	63.9	88.5	89.0
	PBE0	sp- > lp	43.9	61.3	80.0	51.7
		lp- > sp	50.7	81.6	98.1	100.9
	rSCAN	sp- > lp	44.0	60.4	77.3	62.0
		lp- > sp	48.9	75.7	92.1	101.8
	ωB97X-2	sp- > lp	41.0	60.3	69.2	105.1
		lp- > sp	34.6	46.2	76.9	91.0
	revDSD-PBEP86-D4	sp- > lp	39.7	62.8	80.8	89.7
		lp- > sp	39.7	57.7	82.0	93.6
	RPA	sp- > lp	39.7	73.1	89.7	132.0
		lp- > sp	32.0	39.7	71.8	92.3

following the ordering of Kr/MFU-4 < Xe/MFU-4 < Kr/MFU-4-Br < Xe/MFU-4-Br.

Furthermore, the activation energy of the herein studied systems was compared to previously reported values for other systems (Table S18).[10,11] Figure 5 illustrates the relationship between the activation energy and the guest-pore aperture size ratio, serving as a useful tool to predict properties of other systems in terms of effective gas trapping.

Gas diffusion in MOF crystals has generally two main components: diffusion within the MOF crystal and diffusion at the surface. However, since herein the diffusion of the guest through the network is extremely slow (taking up to several weeks), the contribution of surface diffusion becomes negligible in this case. Therefore, under these circumstances, the experimentally obtained activation energy data can be compared to the theoretical data presented in the next chapter, which focuses solely on the guest movement through the network.

Computational Studies

In our previous study on kinetic trapping of xenon in MFU-4,[9] classical molecular dynamics simulations using a reparametrized universal force field and assuming an NVT ensemble were performed for MFU-4 loaded with 15 Xe atoms in the central pore. Even though a temperature range of 200 K to 450 K was investigated, hopping from void to void for Xe in MFU-4 was found only scarcely even for sampling times of 30 ns. Diffusion of Xe through the network structure was thus computationally shown to be very slow in line with the concept of kinetic trapping. Nudged-elastic band (NEB) computations enabled to predict an activation barrier of 66 kJ mol^{-1} for Xe diffusion at GGA level of accuracy using the PBEsol functional and including dispersion corrections as suggested by Tkatchenko and Scheffler.[25] Analogous computations for moving a Kr atom from the large to the small pore of MFU-4 resulted in an activation barrier of 46 kJ mol^{-1} (Table 3).

In the current study, to estimate the energy barriers that prevent gas release, we performed, on the one hand, nudged elastic band (NEB) computations at the moderate cost of GGA density functional theory and, on the other hand, assessed accuracy of the so-obtained NEB trajectories through further single-point computations at the higher accuracy and cost of hybrid, meta-GGA and double hybrid density functionals. An overview on the so-obtained activation energies is summarized in Table 3; corresponding potential energy profiles are visualized in Figure 7.

For the NEB computations, experimental crystal structures of both MFU-4 and MFU-4-Br were first optimized using the PBEsol functional[26] with D3 dispersion correction,[27] DZVP-MOLOPT-SR basis set,[28] and the Goedecker–Teter–Hutter pseudopotentials.[29] The optimized cubic unit cells with a resulting lattice constant of 21.61 Å for MFU-4 and of 21.66 Å for MFU-4-Br, and thereon based theoretical pore apertures of 2.48 Å and 2.19 Å, respectively, are in agreement with the experimental reference values given in Table 1.

Based on the optimized unit cell structures, NEB computations were carried out with consistent computational setup, thus implying the PBEsol functional.[26] The trajectory of the modeled gas diffusion path through the framework structure is exemplarily shown for Xe in MFU-4 in Figure 6: Starting from a structure where Xe is in the middle of the large void of 11.94 Å (left frame), the gas atom passes to the much smaller pore of 3.9 Å through a four-fold coordinated window of halogen atoms, in this case of chlorine atoms colored in green (middle frame). Passing in a reverse sense from the small to the large void, the Xe atom is finally back in the large void (right frame).

The potential energy profiles of Figure 7 correspond to the outlined NEB trajectory: The profile includes two peaks corresponding to the situations where the noble gas atom passes through the halogen window, going from either large to small pore (left peak) or from small to large pore (right peak). Activation energies from large pore to small pore are found to be largest and therefore represent the decisive activation barrier height. In summary, the results indicate an activation energy of 63.9 and 42.9 kJ mol^{-1} for Xe and Kr gases in MFU-4, and of 89.0 and 88.5 kJ mol^{-1} for Xe and Kr in MFU-4-Br, respectively (see also Table 3). The PBEsol results thus imply an ordering and trend in activation energies that follows Kr&MFU-4 < Xe&MFU-4 < Kr&MFU-4-Br ≈ Xe&MFU-4-Br, agreeing with the calculated guest to host ratios (Table 1) and with experimental data.

PBEsol barrier heights were furthermore assessed by increasing the accuracy to meta-GGA, hybrid and double-hybrid density functionals (DHDFs). To keep balance between methodological and basis-set incompleteness error, basis sets were

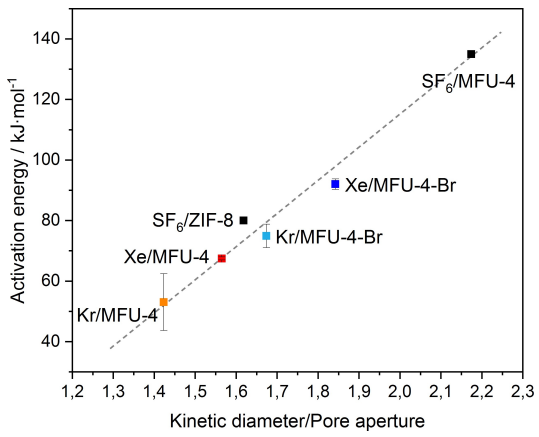

Figure 5. A graphical representation of the relationship between the guest-pore aperture size ratio and the experimentally determined activation energy barrier of the guest release for different systems.

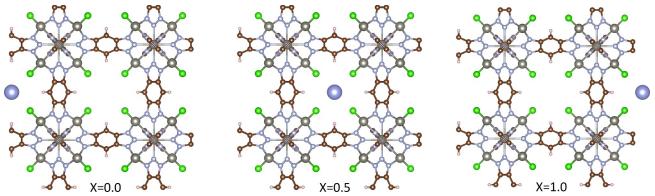

Figure 6. The initial, middle and final configurations along the Xe diffusion path from large to small pore in MFU-4 as simulated with NEB computations.

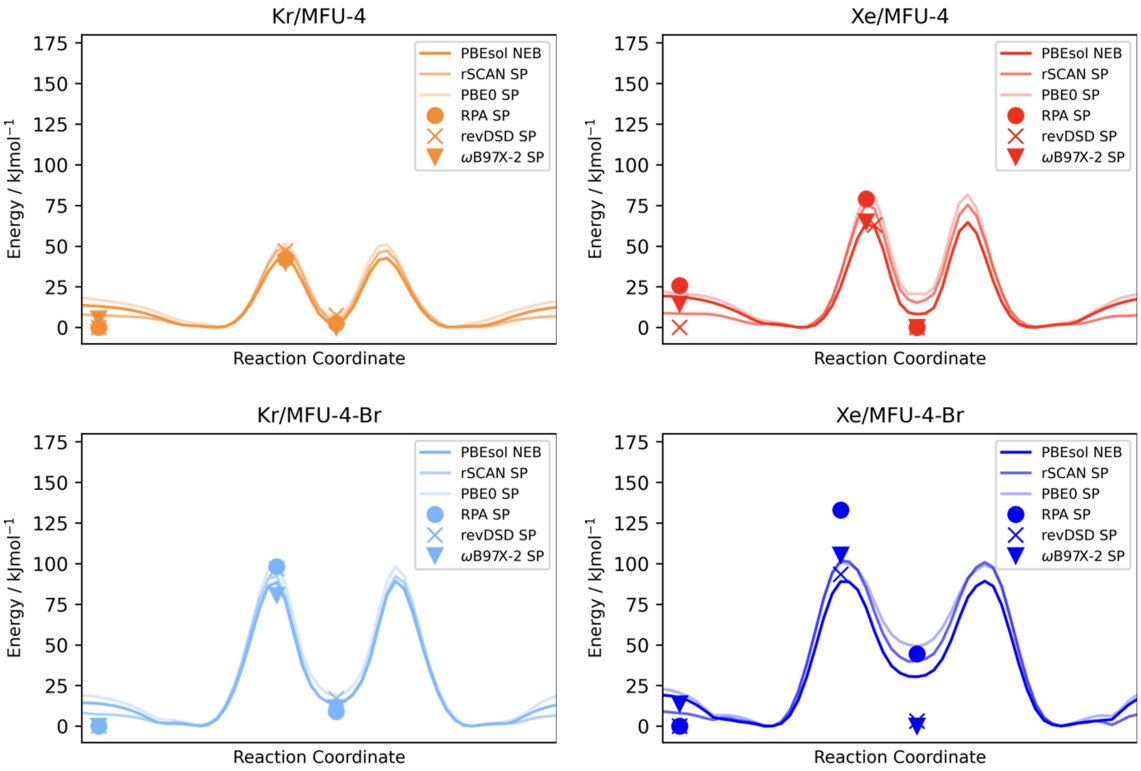

Figure 7. Potential energy profiles of the gas-MOF pairs determined with PBEsol functional using the nudged elastic band method and PBE0 and rSCAN single-point energies based on the PBEsol optimized beads. Further ωB97X-2 (triangle), revDSD-PBEP86-D4 (cross), and RPA (circle) single-point energies were computed for PBEsol geometries corresponding to lowest and highest relative energies of the PBEsol NEB paths.

enlarged to triplet-zeta quality. Due to the large unit cell size of the investigated MFU-4-MOFs, it is then no longer feasible to perform geometry optimizations or NEB computations even at hybrid functional level due to the drastically increasing computational costs. The following assessment is thus restricted to computing single-point energies based on the PBEsol optimized structures as obtained from the NEB computations. For the relatively cheap PBE0 hybrid and the rSCAN meta-GGA functional, single-point computations were performed along the entire minimum energy path. When switching to the more cost intensive double hybrid functionals ωB97X-2 and revDSD-PBEP86-D4 as well as when performing RPA computations, reassessment was restricted to few geometries corresponding to highest energy peaks and lowest energy valleys of the NEB paths.

Resulting activation energies of Xe and Kr obtained from PBE0 single-point energies amount up to 81.6 and 50.7 kJ mol^{-1} in MFU-4, and 100.9 and 98.1 kJ mol^{-1} in MFU-4-Br, respectively. The energy profiles obtained from corresponding rSCAN calculations agree with the PBE0 functional results as displayed in Figure 7, with the former yielding slightly higher barrier energies than the latter. The rSCAN barriers were determined to be 75.7 and 48.9 kJ mol^{-1} in MFU-4, and 101.8 and 92.1 kJ mol^{-1} in MFU-4-Br. The overall trend in activation energies is thus correctly predicted with PBE0 and rSCAN, again following the ordering of Kr/MFU-4 < Xe/MFU-4 < Kr/MFU-4-Br < Xe/MFU-4-Br.

The overall trend is confirmed by the double hybrid and RPA computations, with maximum deviations in the barriers listed in Table 3 being smaller than 3.2/−9.2/19.3/−43.0 and 13.3/7.2/−14.8/−40.0 kJ mol^{-1} for the four investigated combinations of Xe-loaded and Kr-loaded MOFs when comparing to PBEsol and experimental results. If ignoring the outliers of −43 and −40 kJ/mol^{-1} corresponding to RPA computations for Xe/MFU-4-Br, the latter two error ranges also reduce to a maximum of −16.1 and −13.1 kJ/mol^{-1}. However, if not comparing largest barriers, but relative energies to the PBEsol reference, both double hybrid and RPA computations indicate larger error ranges for Xe/MFU-4-Br, as visualized in Figure 7. Furthermore, it was found that the energy of the PBEsol-optimized geometry corresponding to the most favorable adsorption site is higher in energy than corresponding energies for the PBEsol-optimized geometries in the middle of the small pore for the ωB97X-2 results of Kr/MFU-4, Xe/MFU-4 and Xe/MFU-4-Br, for revDSD-PBEP86-D4 in the case of Xe/MFU-4 as well as for all RPA computations, thus in contrast to PBEsol predicting the transition from small to large pore to be lower in energy than the reverse passage from large to small pore. Geometry optimizations at corresponding RPA or double-hybrid level, reducing the remaining basis-set incompleteness error or considering a sophisticated description of the exact exchange contribution for RPA could be remedies expected to overcome these artifacts but are beyond the scope of current work.

All barrier energies refer to a temperature of 0 K and a loading of one guest atom, suggesting that the activation energies can change due to the dynamic effects at finite temperature and higher gas loads.

Conclusions

We presented a study on MFU-4 and its isostructural analogue MFU-4-Br as versatile metal–organic frameworks with adjustable pore apertures. These MOFs, composed of benzobistriazole ligands, Zn^{II} cations, and halide side ligands, exhibit large voids and narrow pore openings, offering potential for customizable guest trapping. Gas loading experiments involving xenon and krypton illustrate the impact of the guest-pore aperture size ratio on gas uptake, with higher ratios requiring elevated temperatures for efficient loading. The experimental determination of activation energy for gas release underscores the significance of this ratio. Moreover, the investigation into gas release kinetics over time, particularly under ambient conditions, offers valuable insights into the long-term gas storage and practical applicability of these MOFs. The gradual release of gases, notably observed in xenon-loaded MFU-4 and MFU-4-Br, highlights the potential for controlled gas storage and release, beneficial for various gas capture and delivery applications. Computational studies further validate these findings, offering insights into the gas diffusion mechanisms within the MOF structures.

Experimental

Materials and Methods

The ligand, 1H,5H-benzo(1,2-d:4,5-d′)bistriazole (H_2-BBTA), was synthesized as described previously.[30] All other chemicals were of reagent grade and used as received from the commercial supplier. Fourier-transform infrared spectra were recorded in the range of 180–4000 cm^{-1} or on a Bruker Equinox 55 FT-IR spectrometer equipped with an ATR unit. The intensity of the bands was assigned as strong (s), middle (m) and weak (w). Electron diffraction (3DED) data of MFU-4-Br were collected using a Rigaku XtaLAB Synergy-ED system equipped with a Rigaku HyPix-ED detector and LaB_6 electron source operating at 200 keV ($\lambda = 0.0251$ Å) in a vacuum at ambient temperature with the side entry grid holder. Data collection and processing, i.e., structure refinements, data reductions, and analysis were performed using the Rigaku Oxford Diffraction CrysAlis^{Pro} program package. The shutterless data, 500 frames of 0.2 deg width, was recorded in continuous crystal rotation mode (3D-ED/MED) at the 645 mm detector distance using the selected area configuration. The samples were placed on a standard amorphous carbon on a Cu grid and transferred to a holder at ambient temperature. The initial object search, electron beam sensitivity tests, selection and centering of crystal, and first measurements were performed also at the transfer temperature. Due to the high symmetry of the crystal structures, dataset merging was not required. The collected data was processed and finalized with frame scaling and empirical correction up to 0.7 Å resolution. To verify phase purity of the bulk sample, the structure model obtained from electron diffraction measurements was used as the initial model for the Rietveld method. The powder sample was measured in reflection geometry on a Rigaku SmartLab XE diffractometer, equipped with a PhotonMax Cu rotating anode (X-ray generator: 9 kW, 45 kV, 200 mA) and a HyPiX-3000 2-D detector. Measurement was conducted using an HTK 1200 N Anton Paar Temperature Oven Chamber at 120 °C under vacuum conditions. Prior to data collection, the sample was heated for 4.5 hours at 120 °C. Data were recorded in the 2θ range of 5–90° with an angular step width of 0.01° and a speed of 1 °C min^{-1}. Ambient X-ray powder diffraction (XRPD) patterns were collected using a Seifert XRD 3003 TT diffractometer with a Meteor1D detector using Cu $K\alpha_1$ radiation ($\lambda = 1.54187$). Variable temperature X-ray powder diffraction data were measured in the 5–60° 2θ range under nitrogen atmosphere with an Empyrean (PANalytical) diffractometer equipped with a Bragg–Brentano HD mirror and a PIXcel3D 2×2 detector. The temperature program carried out in 50 °C steps up 700 °C included a heating rate of 0.05 K s^{-1} and then 10 min isothermal between the measurements. The thermogravimetric analysis of the gas loaded samples was performed with a TGA Q500 analyser in the temperature range of 25–600 °C or 25–700 °C under nitrogen atmosphere at a heating rate of 10 K min^{-1}. The temperature modulated thermogravimetric analysis was performed with the same instrument. The measurement was carried out under a helium atmosphere at a heating rate of 1.5 K min^{-1}, amplitude of ±5 °C and period of 200 s. The gas release kinetics at different heating rates was studied with a BelCat-B catalyst analyzer (Bel Japan, Inc.) coupled with a mass spectrometer (OmniStar GSD 320, Pfeiffer Vacuum). The sample was placed between two plugs of quartz wool in a quartz glass reactor and heated up to 300 °C at a constant heating rate (1, 3, 5 or 7 K min^{-1}) under a flow of helium (30 mL min^{-1}). The composition of the exhaust gas was analyzed by a mass spectrometer. SEM micrographs were recorded on a scanning electron microscope (LEO Zeiss, Gemini 982). The structure of MFU-4-Br was elucidated by both electron diffraction measurement and Rietveld refinement (for details see Supporting Information).[21]

MOF Synthesis

MFU-4, $[Zn_5Cl_4(bbta)_3]_n$: The MOF was prepared by microwave-assisted synthesis by upscaling the procedure reported by us previously.[8] A mixture of anhydrous $ZnCl_2$ (340 mg, 2.495 mmol) and H_2-BBTA (100 mg, 0.624 mmol) in DMF (5 mL) was placed in a Pyrex sample tube (30 mL). The reaction mixture was heated in a microwave synthesizer (CEM, Discover S) to 155 °C at 300 W, kept under these conditions for 10 min, and then cooled to ambient temperature. The formed precipitate was isolated by centrifugation, washed with DMF (3×5 mL) and dried in air at ambient conditions to give an off-white crystalline material (166 mg). The reaction was carried out several times to produce enough material and to ensure its reproducibility. Prior to the gas loading experiments, the as-synthetized sample (166 mg) was kept under vacuum at 320 °C for 24 h to remove any solvent molecules from the pores resulting in 122 mg of an activate material (yield: 62 %).

FT-IR: $\nu = 1437$ (w), 1411 (m), 1315 (m), 1212 (s), 1193 (s), 1031 (w), 866 (s), 779 (w), 434 (s), 394 (m), 246 (s), 231 (s) and 213 (s) cm^{-1}.

MFU-4-Br, $[Zn_5Br_4(bbta)_3]_n$: The MOF was prepared following the procedure for MFU-4, except that anhydrous $ZnBr_2$ was used as a metal salt, the reaction time was prolonged to 15 min and the reaction temperature increased to 165 °C (the last two parameters were changed in order to improve the reaction yield and to prepare crystals of similar sizes to MFU-4). $ZnBr_2$ (560 mg, 2.487 mmol) and H_2-BBTA (100 mg, 0.624 mmol) were dissolved in DMF (5 mL) and placed in a Pyrex sample tube (30 mL). The reaction mixture was heated in a microwave synthesizer (CEM, Discover S) to 165 °C at 300 W, kept under these conditions for 15 min, and then cooled to ambient temperature. The formed precipitate was isolated by centrifugation, washed with DMF (3×5 mL) and dried in air at ambient conditions to give an off-white crystalline material (254 mg). The reaction was carried out several times to produce enough material and to ensure its reproducibility. Prior to the gas loading experiments, the as-synthetized sample (254 mg) was kept under vacuum at 320 °C for 24 h to remove any solvent molecules

from the pores resulting in 194 mg of an activate material (yield: 83 %).

FTIR: ν = 1440 (w), 1411 (m), 1312 (m), 1208 (s), 1194(s), 1032(w), 866 (s), 797 (w), 430 (s), 298 (s), 234 (s) and 208 (s) cm^{-1}.

Despite all our effort and varying synthesis conditions (see below), no single crystals larger than 10 μm could be prepared. To prepare large single crystals the following reaction conditions were tested: MW-assisted and solvothermal syntheses; solvent: DMF, DMF-MeOH (from 5 : 1 to 1 : 1), DMF-EtOH (from 5 : 1 to 1 : 1); temperature: 120–180 °C; time: 10–60 min (MW) and 1–7 days (solvothermal); solvent amount: 0.5–5 mL per 10 mg of the H_2bbta ligand. The ligand to metal ratio was kept constant (1 : 4) in all reactions.

Gas Loading

For each experiment, 20–100 mg of the MOF material was placed in a steel vessel constructed from metal tubing attached to a manometer. The vessel was filled either with xenon or krypton gas and kept at desired pressure and temperature for a desired period of time. Upon cooling to ambient temperature, the gas pressure was released, and a small portion of the sample (ca. 5–10 mg) was immediately analyzed with TGA. The precise experimental setup and examples showing that such experiments are reproducible are given in ref. [9,11]

Gas Release

The gas loaded sample was kept in a container exposed to air at ambient conditions, and after a certain period of time, a small amount (ca. 5–10 mg) was taken and analyzed by TGA and XRPD methods.

Computational Studies

Computations were performed with the CP2K program package[31] implying a mixed Gaussian and plane waves framework. Starting from the experimental crystal structures of MFU-4 (CCDC723714) and MFU-4-Br (this work), the unit cell geometries were optimised using the PBEsol functional,[26] DFT-D3[27] van der Waals pair potential to account for dispersion contributions, DZVP-MOLOPT-SR basis set,[28] the Goedecker–Teter–Hutter pseudopotentials[29] and applying the Broyden-Fletcher-Goldfarb-Shanno (BFGS) algorithm within a threshold of 1×10^{-6} hartree in the energy and 4.5×10^{-4} hartree/bohr in the forces. For all calculations, a grid cutoff/relative grid cutoff of 900/80 Ry was used. Input and relevant data files for the computational results presented in this manuscript are available on Materials Cloud, https://archive.materialscloud.org/record/2024.144.

Nudged Elastic Band Calculations

The improved tangent nudged elastic band[32] (IT-NEB) algorithm was used for finding the minimum energy path, which gives the accurate energy and configuration for the saddle point. By measuring the energy difference between the saddle point and the local and global minima, it is possible to determine the activation energy. In a NEB calculation, the lattice constants of the unit cell are kept fixed, however all other degrees of freedom are allowed to relax. The initial (x = 0.0) and the final (x = 1.0) configurations for the NEB method were constructed by placing the guest atom in the middle of the large pore. The algorithm was then requested to interpolate 64 beads in between, with the middle (x = 0.5) configuration being the guest atom in the middle of the small pore (Figure 6). The spring constant for the NEB beads was set as 0.05 in atomic units, with a convergence threshold of 1×10^{-3} hartree/bohr. As for the cell optimizations, the PBEsol functional with D3-correction to account for dispersion was used together with a DZVP-MOLOPT-SR basis set. Core electrons are approximated using Goedecker–Teter–Hutter pseudopotentials.[29]

Single-Point Energy Computations

The performance of generalized gradient approximation (GGA)-based functionals was assessed by increasing the accuracy to meta-GGA, hybrid and double-hybrid density functionals (DHDFs). Performing NEB calculations even at hybrid functional level is very costly for the systems under investigation. Therefore, only single-point energy computations of PBEsol optimized structures along the minimum energy path were performed to assess the hierarchy of the density functionals PBE0,[33] rSCAN,[34] ωB97X-2[35] and revDSD-PBEP86-D4.[36] For highest accuracy, we performed RPA computations.[37] For the assessment, basis-set size was increased from double-zeta to triple-zeta quality choosing a TZV2P basis for the PBE0 and rSCAN single-point energy computations and a ccGRB-T basis for the ωB97X-2, revDSD-PBEP86-D4 and RPA computations, respectively. RPA basis-set convergence was extrapolated based on results for ccGRB-D and ccGRB-T basis sets to get an estimate for the RPA basis-set incompleteness error. Furthermore, computations for the DHDFs ωB97X-2, revDSD-PBEP86-D4 and for RPA were performed with a threshold of 10^{-9} a.u. for the Schwartz integral screening and a wave function grid of 150 Ry for the correlation contribution. Cutoffs for exchange were checked to be converged by increasing the wave function cutoff from 150 Ry to 200 Ry leading to negligible differences in the total energies. Convergence for the cutoff radius for the exchange contribution was checked for values between 8 to 10 Angstrom, resulting in consistent and thus converged energies.

Acknowledgements

B. S. G., A.-S. H. and J. H. gratefully acknowledge computational resources provided by production project s1195 at the Swiss National Supercomputing Center (CSCS). Open Access funding enabled and organized by Projekt DEAL.

Conflict of Interests

The authors declare no conflict of interest.

Data Availability Statement

The data that support the findings of this study are available in the supplementary material of this article.

Keywords: Metal–organic framework · Gas storage · Crystal engineering · Electron diffraction · Computational modeling

[1] O. M. Yaghi, M. J. Kalmutzki, C. S. Diercks, *Introduction to Reticular Chemistry: Metal–Organic Frameworks and Covalent Organic Frameworks*, Wiley-VCH, Weinheim **2019**.

[2] Jeong, B. G. Hauser, C. E. Wilmer, A. A. Sarjeant, R. Q. Snurr, S. T. Nguyen, A. Ö. Yazaydın, J. T. Hupp, *J. Am. Chem. Soc.* **2012**, *134*, 15016–15021.
[3] I. M. Hönicke, I. Senkovska, V. Bon, I. A. Baburin, N. Bönisch, S. Raschke, J. D. Evans, S. Kaskel, *Angew. Chem. Int. Ed.* **2018**, *57*, 13780–13783.
[4] a) H. Furukawa, K. E. Cordova, M. O'Keeffe, O. M. Yaghi, *Science* **2013**, *341*, 1230444; b) R. B. Lin, S. C. Xiang, H. B. Xing, W. Zhou, B. L. Chen, *Coord. Chem. Rev.* **2019**, *378*, 87–103; c) H. Daglar, H. C. Gulbalkan, G. Avci, G. O. Aksu, O. F. Altundal, C. Altintas, I. Erucar, S. Keskin, *Angew. Chem.-Int. Ed.* **2021**, *60*, 7828–7837; d) C. Jiang, X. Wang, Y. Ouyang, K. Lu, W. Jiang, H. Xu, X. Wie, Z. Wang, F. Dai, D. Sun, *Nanoscale Adv.* **2022**, *4*, 2077–2089.
[5] a) X. Cui, K. Chen, H. Xing, Q. Yang, R. Krishna, Z. Bao, H. Wu, W. Zhou, X. Dong, Y. Han, B. Li, Q. Ren, M. J. Zaworotko, B. Chen, *Science* **2016**, *353*, 141–144; b) J. Li, P. M. Bhatt, J. Li, M. Eddaoudi, Y. Liu, *Adv. Mater.* **2020**, *32*, 2002563; c) Z. Ji, H. Wang, S. Canossa, S. Wuttke, O. M. Yaghi, *Adv. Funct. Mater.* **2020**, *30*, 2000238; d) K. Chen, S. H. Mousavi, R. Singh, R. Q. Snurr, G. Li, P. A. Webley, *Chem. Soc. Rev.* **2022**, *51*, 1139–1166; e) J. Wang, Y. Zhang, Y. Su, X. Liu, P. Zhang, R. B. Lin, S. Chen, Q. Deng, Z. Zeng, S. Deng, B. Chen, *Nat. Commun.* **2022**, *13*, 200; f) W. Xie, L. Yang, J. Zhang, X. Zhao, *Chem. Eur. J.* **2023**, *29*, e202300158; g) W.-L. Li, Q. Shuai, J. Yu, *Small* **2024**, 2402783, https://doi.org/10.1002/smll.202402783.
[6] Z. Guo, H. Wu, G. Srinivas, Y. Zhou, S. Xiang, Z. Chen, Y. Yang, W. Zhou, M. O'Keeffe, B. Chen, *Angew. Chem. Int. Ed.* **2011**, *50*, 3178–3181.
[7] T. M. McDonald, J. A. Mason, X. Kong, E. D. Bloch, D. Gygi, A. Dani, V. Crocella, F. Giordanino, S. O. Odoh, W. S. Drisdell, B. Vlaisavljevich, A. L. Dzubak, R. Poloni, S. K. Schnell, N. Planas, K. Lee, T. Pascal, L. F. Wan, D. Prendergast, J. B. Neaton, B. Smit, J. B. Kortright, L. Gagliardi, S. Bordiga, J. A. Reimer, J. R. Long, *Nature* **2015**, *519*, 303–308.
[8] S. Biswas, M. Grzywa, H. P. Nayek, S. Dehnen, I. Senkovska, S. Kaskel, D. Volkmer, *Dalton Trans.* **2009**, 6487–6495.
[9] H. Bunzen, F. Kolbe, A. Kalytta-Mewes, G. Sastre, E. Brunner, D. Volkmer, *J. Am. Chem. Soc.* **2018**, *140*, 10191–10197.
[10] H. Bunzen, A. Kalytta-Mewes, L. van Wüllen, D. Volkmer, *Beilstein J. Nanotechnol.* **2019**, *10*, 1851–1859.
[11] K. Heinz, S. M. J. Rogge, A. Kalytta-Mewes, D. Volkmer, H. Bunzen, *Inorg. Chem. Front.* **2023**, *10*, 4763–4772.
[12] a) W. Lu, Z. Wie, Z.-Y. Gu, T.-F. Liu, J. Park, J. Park, J. Tian, M. Zhang, Q. Zhang, T. Gentle III, M. Bosch, H.-C. Zhou, *Chem. Soc. Rev.* **2014**, *43*, 5561–5593; b) M. J. Kalmutzki, N. Hanikel, O. M. Yaghi, *Sci. Adv.* **2018**, *4*, eaat9180; c) Z. Chen, H. Jiang, M. Li, M. O'Keeffe, M. Eddaoudi, *Chem. Rev.* **2020**, *120*, 8039–8065; d) H. Lyu, Z. Ji, S. Wuttke, O. M. Yaghi, *Chem* **2020**, *6*, 2219–2241; e) A. Ejsmont, J. Andreo, A. Lanza, A. Galarda, L. Macreadie, S. Wuttke, S. Canossa, E. Ploetz, J. Goscianska, *Coord. Chem. Rev.* **2021**, *430*, 213655.
[13] a) D. Denysenko, M. Grzywa, M. Tonigold, B. Streppel, I. Krkljus, M. Hirscher, E. Mugnaioli, U. Kolb, J. Hanss, D. Volkmer, *Chem. Eur. J.* **2011**, *17*, 1837–1848; b) P. Schmieder, M. Grzywa, D. Denysenko, M. Hambach, D. Volkmer, *Dalton Trans.* **2015**, *44*, 13060–13070.
[14] a) J. Teufel, H. Oh, M. Hirscher, M. Wahiduzzaman, L. Zhechkov, A. Kuc, T. Heine, D. Denysenko, D. Volkmer, *Adv. Mater.* **2013**, *25*, 635–639; b) I. Weinrauch, I. Savchenko, D. Denysenko, S. M. Souliou, H.-H. Kim, M. Le Tacon, L. L. Daemen, Y. Cheng, A. Mavrandonakis, A. J. Ramirez-Cuesta, D. Volkmer, G. Schütz, M. Hirscher, T. Heine, *Nat. Commun.* **2017**, *8*, 14496; c) B. Paschke, D. Denysenko, B. Bredenkötter, G. Sastre, A. Wixforth, D. Volkmer, *Chem. Eur. J.* **2019**, *25*, 10803.
[15] a) D. Denysenko, T. Werner, M. Grzywa, A. Puls, V. Hagen, G. Eickerling, J. Jelic, K. Reuter, D. Volkmer, *Chem. Commun.* **2012**, *48*, 1236–1238; b) D. Denysenko, M. Grzywa, J. Jelic, K. Reuter, D. Volkmer, *Angew. Chem. Int. Ed.* **2014**, *53*, 5832–5836; c) D. Denysenko, J. Jelic, K. Reuter, D. Volkmer, *Chem. Eur. J.* **2015**, *21*, 8188–8199; d) D. Denysenko, J. Jelic, O. V. Magdysyuk, K. Reuter, D. Volkmer, *Microporous Mesoporous Mat.* **2015**, *216*, 146–150; e) D. Denysenko, D. Volkmer, *Faraday Discuss.* **2017**, *201*, 101–112; f) A. M. Wright, C. Sun, M. Dincă, *J. Am. Chem. Soc.* **2021**, *143*, 681–686; g) Y. Yabuuchi, H. Furukawa, K. M. Carsch, R. A. Klein, N. V. Tkachenko, A. J. Huang, Y. Cheng, K. M. Taddei, E. Novak, C. M. Brown, M. Head-Gordon, J. R. Long, *J. Am. Chem. Soc.* **2024**, *146*, 22759–22776.
[16] a) E. D. Metzger, C. K. Brozek, R. J. Comito, M. Dincă, *ACS Cent. Sci.* **2016**, *2*, 148–153; b) R. J. Comito, K. J. Fritzsching, B. J. Sundell, K. Schmidt-Rohr, M. Dincă, *J. Am. Chem. Soc.* **2016**, *138*, 10232–10237; c) R. J.-C. Dubey, R. J. Comito, Z. Wu, G. Zhang, A. J. Rieth, C. H. Hendon, J. T. Miller, M. Dincă, *J. Am. Chem. Soc.* **2017**, *139*, 12664–12669; d) E. D. Metzger, R. J. Comito, C. H. Hendon, M. Dincă, *J. Am. Chem. Soc.* **2017**, *139*, 757–762; e) M. R. Mian, H. Chen, R. Cao, K. O. Kirlikovali, R. Q. Snurr, T. Islamoglu, O. K. Farha, *J. Am. Chem. Soc.* **2021**, *143*, 9893–9900.
[17] A. W. Wright, Z. Wu, G. Zhang, J. L. Mancuso, R. J. Comito, R. W. Day, C. H. Hendon, J. T. Miller, M. Dincă, *Chem* **2018**, *4*, 2894–2901.
[18] R. Ettlinger, M. Sönksen, M. Graf, N. Moreno, D. Denysenko, D. Volkmer, K. Kerl, H. Bunzen, *J. Mater. Chem. B* **2018**, *6*, 6481–6489.
[19] a) Z. Cai, C. E. Bien, Q. Liu, C. R. Wade, *Chem. Mater.* **2020**, *32*, 4257–4264; b) Q. Liu, S. G. Cho, J. Hilliard, T.-Y. Wang, S.-C. Chien, L.-C. Lin, A. C. Co, C. R. Wade, *Angew. Chem. Int. Ed.* **2023**, *62*, e202218854.
[20] H. Bunzen, M. Grzywa, M. Hambach, S. Spirkl, D. Volkmer, *Cryst. Growth Des.* **2016**, *16*, 3190–3197.
[21] Deposition numbers 238549 (for MFU-4-Br, Rietveld refinement) and 238548 (for MFU-4-Br, electron diffraction) contain the supplementary crystallographic data for this paper. These data are provided free of charge by the joint Cambridge Crystallographic Data Centre and Fachinformationszentrum Karlsruhe Access Structures service.
[22] a) BIOVIA, *Dassault Systèmes, Materials Studio*, Dassault Systèmes, San Diego **2018**; b) S. J. Clark, M. D. Segall, C. J. Pickard, P. J. Hasnip, M. I. J. Probert, K. Refson, M. C. Payne, *Z. Kristallogr.* **2005**, *220*, 567–570.
[23] D. W. Breck, *Zeolite Molecular Sieves: Structure, Chemistry and Use*, John Wiley & Sons Inc., New York **1974**, p. 677.
[24] R. L. Blaine, B. K. Hahn, *J. Therm. Anal. Calorim.* **1998**, *54*, 695–704.
[25] A. Tkatchenko, M. Scheffler, *Phys. Rev. Lett.* **2009**, *102*, 073005.
[26] J. P. Perdew, A. Ruzsinszky, G. I. Csonka, O. A. Vydrov, G. E. Scuseria, L. A. Constantin, X. Zhou, K. Burke, *Phys. Rev. Lett.* **2008**, *100*, 136406–136409.
[27] S. Grimme, S. Ehrlich, L. Goerigk, *J. Comput. Chem.* **2011**, *32*, 1456–1465.
[28] J. VandeVondele, J. Hutter, *J. Chem. Phys.* **2007**, *127*, 114105.
[29] S. Goedecker, M. Teter, J. Hutter, *Phys. Rev. B* **1996**, *54*, 1703–1710.
[30] H. Hart, D. Ok, *J. Org. Chem.* **1986**, *51*, 979–986.
[31] T. D. Kühne, M. Iannuzzi, M. D. Ben, et al., *J. Chem. Phys.* **2020**, *152*, 194103.
[32] G. Henkelman, H. Jónsson, *J. Chem. Phys.* **2000**, *113*, 9978.
[33] C. Adamo, V. Barone, *J. Chem. Phys.* **1999**, *110*, 6158.
[34] P. Hao, J. Sun, B. Xiao, A. Ruzsinszky, G. I. Csonka, J. Tao, S. Glindmeyer, J. P. Perdew, *J. Chem. Theory Comput.* **2013**, *9*, 355–363.
[35] J. D. Chai, M. Head-Gordon, *J. Chem. Phys.* **2009**, *131*, 174105.
[36] G. Sandra, N. Sylvetsky, J. M. L. Martin, *J. Phys. Chem. A* **2019**, *123*, 5129–5143.
[37] H. Eshuis, J. E. Bates, F. Furche, *Theor. Chem. Acc.* **2012**, *131*, 1084.

Manuscript received: September 25, 2024
Accepted manuscript online: November 21, 2024
Version of record online: December 11, 2024